PCCP

PAPER

View Article Online
View Journal | View Issue

Cite this: *Phys. Chem. Chem. Phys.*, 2026, **28**, 10414

Dissociation of halogenated deoxyuridines as potential radiosensitizers, induced by deep inner-shell photoionization – experiment and modeling

Kerttu-Inkeri Pusa,*[a] Edwin Kukk,[a] Marta Berholts,[b] Tatiana Marchenko,[cd] Iyas Ismail,[cd] Denis Céolin,[d] Marc Simon[cd] and Oksana Travnikova*[cd]

Halogenated nucleosides are known candidates for enhancing X-ray damage in radiotherapy of tumors and are also excellent model systems for investigating molecular and charge dynamics following deep inner-shell ionization. We carried out electron–multi-ion coincidence measurements with two gas-phase halogenated deoxyuridine derivatives – 5-iodo-4-thio-2′-deoxyuridine (ISDU) and 5-bromo-4-thio-2′-deoxyuridine (BrSDU). We report the fragmentation patterns and kinetic energies of ions in coincidence with the I 2p, Br 2p and S 1s photoelectrons, complementing the experiment with molecular mechanics simulations and developing the parametric, stochastic model further. This work demonstrates the applicability of the multiparticle energy- and momentum-resolved coincidence technique to the relatively unexplored regime of incomplete Coulomb explosion of a biomolecular system charged up by deep inner-shell Auger cascades. Simulations of the incomplete Coulomb explosions are carried out to compare with, and complement the experimental data. Their good overall agreement shows the expected trend of more energetic Coulomb explosions and an increased degree of atomization as deeper atomic inner-shells are ionized. The presented data on ion abundances and kinetic energies extend beyond these general predictions, providing essential input for modeling the subsequent damage propagation into the surrounding environment – an aspect directly related to the radiosensitizing properties. Some observables, such as the kinetic energies of halogen ions, are particularly sensitive to the interplay of the charge and nuclear dynamics and provide valuable benchmarks for model development.

Received 15th December 2025,
Accepted 13th February 2026

DOI: 10.1039/d5cp04872a

rsc.li/pccp

1 Introduction

Experimental studies of halogenated organic molecules present a rich source of information on the interaction of light with small quantum systems. Heavy halogen atoms create absorption hotspots in the organic compound for suitable X-ray energies having a large cross-section for core or deep inner-shell ionization. The initial deep inner-shell vacancies trigger an electronic relaxation cascade, involving Auger decay and other electron–electron processes, resulting in a high overall charge build-up.[1–10] This electron dynamics is initially localized at the halogen atom. When the valence electrons become involved, at the later stages of the cascades, the entire compound acts as an electron reservoir to sustain the cascade, and the positive charge starts to spread over the entire molecule. This initiates a concurrent fragmentation dynamics (FD) of the molecule and, for the highly charged states, leads to Coulomb explosion (CE) of the molecule.

Here, we investigate two 28-atom halogenated biomolecules: 5-iodo-4-thio-2′-deoxyuridine and 5-bromo-4-thio-2′-deoxyuridine, shown in Fig. 1 and from here on, referred to as ISDU and BrSDU, respectively. These molecules are of both fundamental and applied interest. The charge build-up process described above results in accumulated charge insufficient for ionizing all constituent atoms – the condition we will refer here as the incomplete Coulomb explosion (ICE). While the ICE regime would be the most common following X-ray interactions with *e.g.* halogenated biomolecular constituents, it is little studied with scarce experimental data. Also the numerical modeling has been concentrated rather on linking the momentum imaging to the geometrical properties of the target, with essentially instant and complete

[a] *Department of Physics and Astronomy, University of Turku, FI-20014 Turku, Finland. E-mail: kerttu.i.pusa@utu.fi*
[b] *Institute of Physics, University of Tartu, W. Ostwaldi 1, EE-50411 Tartu, Estonia*
[c] *Sorbonne Université, CNRS, UMR 7614, Laboratoire de Chimie Physique-Matière et Rayonnement, F-75005 Paris, France. E-mail: oksana.travnikova@sorbonne-universite.fr*
[d] *Synchrotron SOLEIL, L'Orme des Merisiers, Saint-Aubin, F-91192 Gif-sur-Yvette Cedex, France*

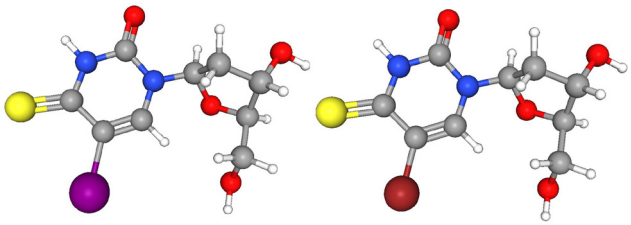

Fig. 1 Sample molecules, 5-iodo-4-thio-2′-deoxyuridine (ISDU) and 5-bromo-4-thio-2′-deoxyuridine (BrSDU), studied.

atomization.[11,12] The present study both provides experimental data and investigates numerical modeling for ICE processes.

As for the applied aspect, ISDU and BrSDU have been proposed as possible radiosensitizers (RS) in radiotherapy of tumors.[13,14] The former showed clear RS properties, while the latter had no RS effect.[13,14] Experimental and modeled data can shed light on the different efficacies of these chemically and structurally similar compounds. Such investigations also contribute to the general understanding of the processes involved in radiosensitization.

The new MUSTACHE electron–multi-ion coincidence setup[15] was used to selectively probe the iodine 2p, bromine 2p and sulfur 1s inner shells and to investigate FD associated with these ionizations. Regarding the RS properties, this is a significant advance compared to earlier studies using soft X-rays, since the relevance to the action of hard medical X-rays is much more direct. Targeting the even deeper K-shell of iodine and bromine in the molecule might appear to be even more directly relevant to medical X-rays. However, the K-shell vacancies in heavy atoms are predominantly filled by fluorescence, transferring the vacancy to the L-shell without increasing charge. In iodine, for instance, fluorescence accounts for about 88% of K-shell decays.[16] Thus, the eventual FD, starting from either the K or the L-shell ionization, is expected to be quite similar.[17]

The coincidence data contain a large amount of information not only on single ions but on their correlations in terms of yields, energies and in the momentum space. However, in a large system, these correlations are not clear-cut and therefore we concentrate here on the primary information in the form of various ion yields and energetics, with supporting data on ion momentum correlation in specific instances. While the experiment provides a wealth of information on the ICE events, their complete characterization – detection of all the charged fragments in coincidence – is not feasible. Therefore, the experimental results can be combined with theoretical and experimental information available from literature and complemented with model simulations, to create a more complete picture of the deep inner-shell ionization in halogenated organic compounds. Here, we employ the Stochastic, Parametric Charge-Hopping Molecular Mechanics (SPCHMM) model to simulate both the charge and the molecular break-up dynamics. With tunable parameters, the model essentially provides a fit to the experimental data that suggests the type of scenario that is appropriate for the deep inner-shell ionization conditions in a sizable organic molecule.

In the following, we review briefly previous studies related to ISDU and BrSDU, present the experimental setup and the experimental findings. We then introduce the molecular mechanics model and compare its results with the experiment. The SI adds considerable detail on the sample, its possible thermal degradation, and on handling the contaminants. Details of the procedures used in data analysis are also described in the SI. Additional data on the results of numerical modeling (ion energies, abundances, momentum correlations) is provided by the SI.

1.1 Prior relevant studies of the radiosensitizing (RS) properties

In radiotherapy, damage to DNA arises directly from its interaction with ionizing radiation or indirectly as radiation interacts with surrounding molecules, predominantly water, releasing hydroxyl radicals and hydrated electrons.[18,19] The former can damage native DNA, but in tumor cells, which are typically oxygen-deprived (hypoxic), their destructive ability is reduced.[14,19,20] The hydrated electrons, on the other hand, seen as playing a negligible role in damaging the native DNA, can become an important factor when certain RS molecules are incorporated into the DNA.[14,20,21] In addition, incorporating heavy-element-containing RS (such as ISDU) into the DNA enhances the direct radiation damage as these molecules act as absorption hotspots.

Numerous studies, such as ref. 22–28, have investigated halogenated nucleosides and nucleobases, particularly for their potential use as RS drugs. Derivatives similar to ISDU and BrSDU, such as 5-iodo-2′-deoxyuridine (IDU) and 5-bromo-2′-deoxyuridine (BrDU) have been studied extensively, and are known to be efficient RSs.[20,27,29,30] BrSDU and ISDU were synthesized by Xu *et al.* in 2004[31] and Zhang *et al.* in 2014,[32] respectively. Substituting one oxygen in the uracil with a sulfur atom causes the absorption maximum of the 2′-deoxyuridine molecule to shift to the UVA region.[33] Indeed, ISDU and BrSDU are known to be photosensitizers.[32] However, their RS abilities are still under investigation. Interestingly, ISDU was found to be a potential RS by Makurat *et al.*,[13] whereas in a following study by Spisz *et al.*,[14] BrSDU exhibited no RS properties. The key difference between the radiolysis products of ISDU and BrSDU was in the dissociative electron attachment (DEA) channel.[14] Aqueous solution of ISDU was irradiated with X-rays to study effects of solvated electrons. One of the main radiolysis products was 4-thio-2′-deoxyuridine radical (SDU$^{\bullet}$) that, according to quantum chemical calculations, formed after an electron attached to the neutral parent molecule that consequently dissociated to I^- and SDU$^{\bullet}$ radical.[13] In a similar radiolysis study of BrSDU, no DEA products were observed – *i.e.* no SDU$^{\bullet}$ radical was formed.[14]

A nucleoside radical, such as SDU$^{\bullet}$, is typically responsible for the damage caused to DNA.[20] For this reason, Spisz *et al.* attribute the differences in the RS abilities of ISDU and BrSDU to the lack of DEA product in the radiolysis of the latter.[14] There is also apparent discrepancy in the RS efficiency between

BrSDU and BrDU; BrDU is one of the most studied DEA-type RSs[34] whereas BrSDU shows no RS properties.

Most studies focusing on the RS properties of modified nucleosides investigate the effects of slow electrons *i.e.* DEA effects, as described above, because they are considered to be the most relevant in actual biological systems.[14] Izadi *et al.*,[35] while investigating DEA to BrSDU in gas phase, observed indications of thermal decomposition of the sample, namely cleavage of the glycosidic bond between the nucleobase (BrSU) and the deoxyribose (D) moiety. This is significant, as the possibility of thermal decomposition has to be considered also in the present study. Izadi *et al.* concluded (based on quantum chemical calculations) that the deoxyribose moiety does not significantly affect the energetics of the process where a bromine anion is released from the parent and, since this process is associated with the RS properties of modified nucleosides,[14] suggested that BrSU can, to some extent, be used as a model compound for BrSDU. Saqib *et al.* studied DEA to ISDU in gas phase.[36] They carried out electron impact ionization measurements at 110 °C to study possible thermal degradation of the sample and did not report any, in contrast to the case of BrSDU. Even so, they also suggest that the deoxyribose moiety does not play a significant role in the DEA process.

Molecular dissociation of ISDU and BrSDU as a direct result of photoabsorption has not been studied, to the best of our knowledge. Some of the closest nucleoside and nucleobase derivatives whose photofragmentation patterns have been investigated include halogenated uracils,[37–39] thiouracils,[40–42] uridine,[43,44] and thymidine.[43,45,46] The effects of the C 1s core-level photoionization have been studied for thymine,[37] 5-bromouracil,[37] uridine[44] and thymidine.[45] Molecular fragmentation dynamics in 5-iodouracil has been also induced by multiphoton I 2p ionization using free electron laser.[38,39] Valence photoionization has been studied for thymidine and uridine with photon energies ranging from 10 eV to 50 eV,[43,45,46] and also for thionated uracils: for 2-thiouracil up to 15 eV[41] and for 4-thiouracil, using molecular dynamics simulations over 12–16 eV photon energies.[42] Additionally, thymidine has been studied as a part of an oligonucleotide: in ref. 47, fragmentation of a thymidine including oligonucleotide was followed from valence to the C, N and O 1s ionizations. Recently, Svensson *et al.*[48] studied fragmentation of an oligonucleotide that incorporated iodinated thymidine – they targeted specifically the 2p orbital of iodine. This study was limited to detecting only fragments with mass-to-charge ratio above 60 while our data on isolated RS molecules provides information on much smaller fragments, including H^+, making the two approaches complementary.

2 Experimental

The experiment was performed at the SOLEIL Synchrotron, France, on the GALAXIES beamline,[49] where linearly polarized light is provided by a U20 undulator and monochromatized by a Si(111) double crystal monochromator. The samples were introduced into the interaction region as molecular jet and the

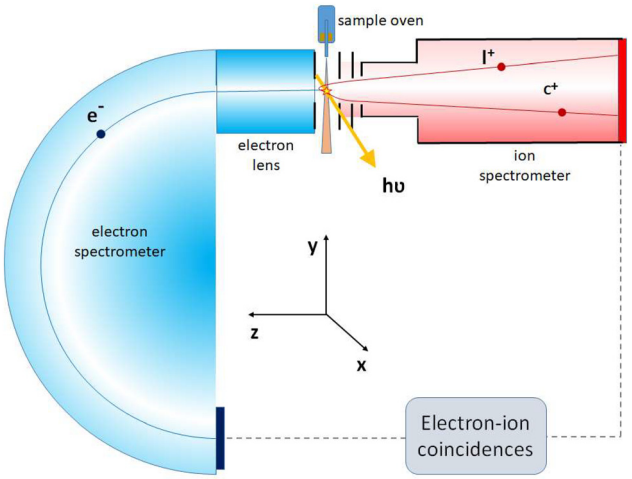

Fig. 2 Schematics of the MUSTACHE electron–ion coincidence setup.

electron-energy-resolved electron–multi-ion coincidence (PEPIPICO) data was recorded using the MUSTACHE set-up (see Fig. 2).[15] The MUSTACHE (MUlti-STep photofragmentation studies by Auger electron–ion Coincidences using High-Energy photons) setup is a high-resolution electron–multi-ion coincidence system optimized for gas-phase experiments in the tender (~2–10 keV) range and above. The system integrates a high-resolution Scienta Omicron DA20(R) high energy DLD hemispherical electron analyzer with a modified Wiley–McLaren-type ion time-of-flight (TOF) spectrometer, enabling coincidence measurements with photo- and Auger electrons. The coincidence multi-ion acquisitions are triggered by a detected electron in the kinetic energy range to which the electron spectrometer is tuned. The ion flight times and hit positions are then recorded while blocking new electron detection, creating data for a single electron–multi-ion coincidence event.

The ion extraction voltages of ±460 V were applied across the sample region, and −1750 V acceleration voltage was applied. The lens voltage was −175 V. In the pulsed ion extraction field mode, the false coincidences – combinations of ions and electrons from unrelated ionization events occurring close in time – are present in the coincidence data. In the MUSTACHE setup, a concurrent set of ion data was recorded using the random triggers that were artificially generated with no actual electron detection. These events, interleaved with true electron triggers, can be assumed to contain only the false coincidences. When producing one- or two-dimensional histograms from the events, histograms generated using the random triggers were subtracted as false coincidence background removal. In the present measurements, the false coincidence ion fraction amongst the analyzed ions was kept at approximately 40%, including the detector noise counts, at which level the subtraction procedure works efficiently.

The I $2p_{3/2}$, Br $2p_{3/2}$ and S 1s photoelectron lines were recorded in the PEPIPICO measurements with a resolution of about 1.0 eV and the photon energies of 4.64 keV, 2.40 keV and 2.58 keV were used, respectively.

The ISDU and BrSDU samples were purchased from Hangzhou Leap Chem Co. with 97% purity (min). The powder samples were

evaporated from a resistively heated crucible at the temperatures of 89 °C (ISDU) and 99 °C (BrSDU). The samples and their possible thermal degradation are discussed in more detail in SI Section S1.

3 Experimental results

3.1 Data analysis

In the electron-energy-resolved PEPIPICO datasets, the flight times and detection coordinates of the fragment ions were recorded together with the coincident photoelectron's kinetic energy (KE). We studied the fragmentation outcomes following the I $2p_{3/2}$ and S 1s photoionization in ISDU and the Br $2p_{3/2}$ and S 1s ionization in BrSDU. An ion TOF spectrum was generated from each PEPIPICO measurement. The spectra, converted to the M/Q-scale, are shown in Fig. 3 and 4, for ISDU and BrSDU, respectively.

As seen from Fig. 3 and 4, the ion TOF peaks are strongly broadened due to the ions' high KE. In order to identify individual ion species, determine their abundance and KE, a more informative representation combines the hit radius of an ion with its TOF as R(TOF) plots. Such plots are shown in Fig. 5 for (a) S 1s and (b) I 2p ionization of ISDU and in Fig. 6 for (a) S 1s and (b) Br 2p ionization of BrSDU. The R(TOF) plots show a characteristic shape for each high-energy ion that peaks (R = max) at the nominal flight time, while the flight paths along the spectrometer's axis (R = 0) give the largest deviation from the nominal TOF. The former corresponds to the initial velocity perpendicular to, and the latter parallel to the spectrometer's axis (Fig. 2). Exceptionally, the hydrogen ions do not present this typical shape, since they are ejected with very high velocity that significantly reduces their transmission to the detector and strongly distorts their R(TOF) shapes making the analysis less straightforward (and thus the H^+ ions are not shown in Fig. 5 and 6). Average transmission for H^+ was estimated by independent methods and was used to correct abundances presented in Table 1 and Fig. 7 (details in SI Section S2.3).

The R(TOF) plots capture not only the ions' M/Q values but also the information needed to obtain their momentum distributions. Fig. 5 and 6 are the basis of our subsequent analysis of the abundances and KEs of individual ionic species. Before presenting the quantitative results, let us compare the main features of the plots starting from the deepest inner-shell ionization. The I 2p ionization of ISDU leads to clear patterns of atomic fragments (Fig. 5b). Among these, C^+ is by far the most prominent, but also the most diffuse, indicating a large spread of the ions' KE distribution. Several changes are immediately apparent when proceeding to the less energetic ionization of S 1s (Fig. 5a) – multiply charged species all but disappear and the atomization is not complete, since molecular fragments can be observed in several TOF regions. Although the plot has lower statistics than that of I 2p, it is nevertheless clear that the molecular fragments contain a range of masses rather than being specific species and have lower KE than the atomic ions. It is also notable that, following the S 1s ionization, the S^+ fragment becomes one of the most prominent. We also note that the S 1s ionization results, as expected for the two very similar molecules, in a very similar fragment composition and KEs for both ISDU (Fig. 5a) and BrSDU (Fig. 6a), with the one apparent difference that the relative abundance of the Br^+ ions is larger than that of the I^+ ions. Going to the Br 2p ionization, which is much less energetic than that of I 2p, we observe (Fig. 6b) again the C^+ ions dominating, and notably the S^+ and N^+ ions are present, contrary to I 2p ionization. Also, the molecular fragments still contribute significantly after the Br 2p ionization.

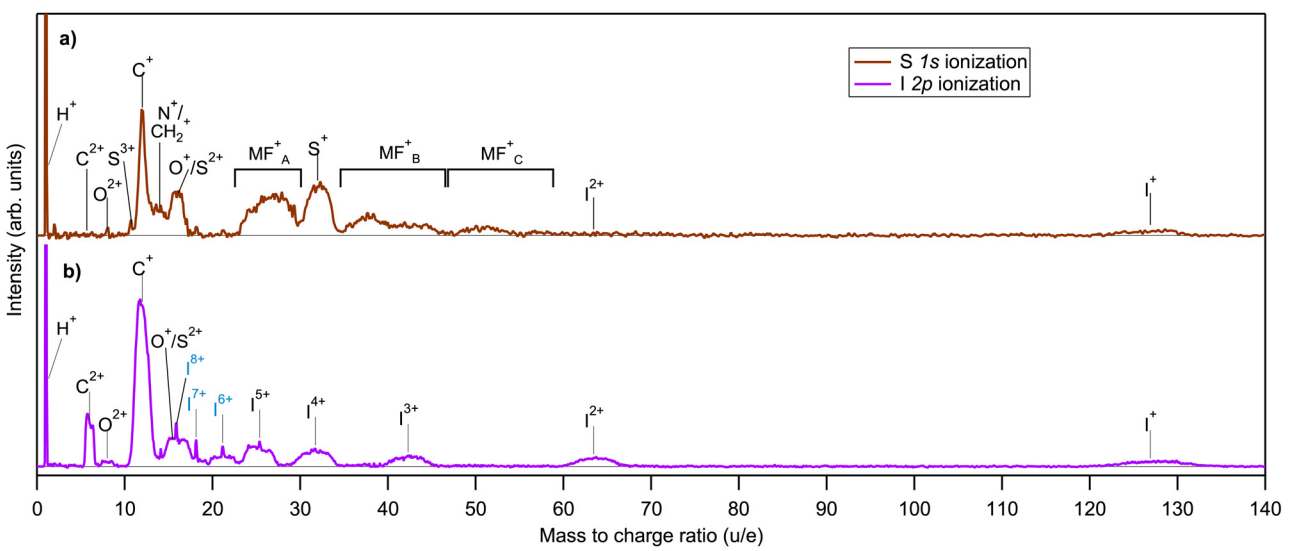

Fig. 3 Ion mass spectra of ISDU measured in coincidence with the S 1s (a) and I $2p_{3/2}$ (b) photoelectrons. False coincidences are subtracted and the spectra are normalized by the height of the I^+ peaks. In addition to the labeled atomic ions, the mass-ranges of significant molecular fragments are marked by $MF_{A,B,C}{}^+$ and $CH_2{}^+$, the latter indistinguishable from atomic N^+. The narrow peaks appearing for highly charged iodine fragments are assigned to the contaminant HI molecule. The I^{6+}–I^{8+} peaks marked in blue are not assigned to ISDU but entirely to contaminant I_2 and HI.

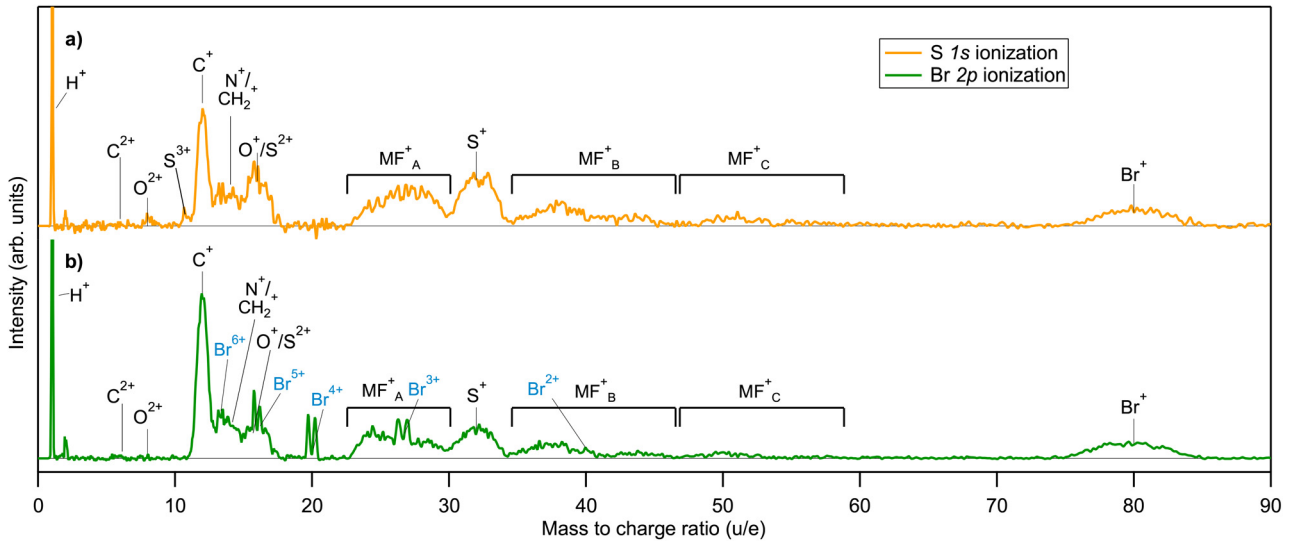

Fig. 4 Ion mass spectra of BrSDU measured in coincidence with the S 1s (a) and Br $2p_{3/2}$ (b) photoelectrons, normalized by the height of the Br^+ peaks. In addition to the labeled atomic ions, the mass-ranges of significant molecular fragments are marked by $MF_{A,B,C}^+$ and CH_2^+. Sharp doublet features Br^{3+}–Br^{6+} are assigned to contaminant HBr.

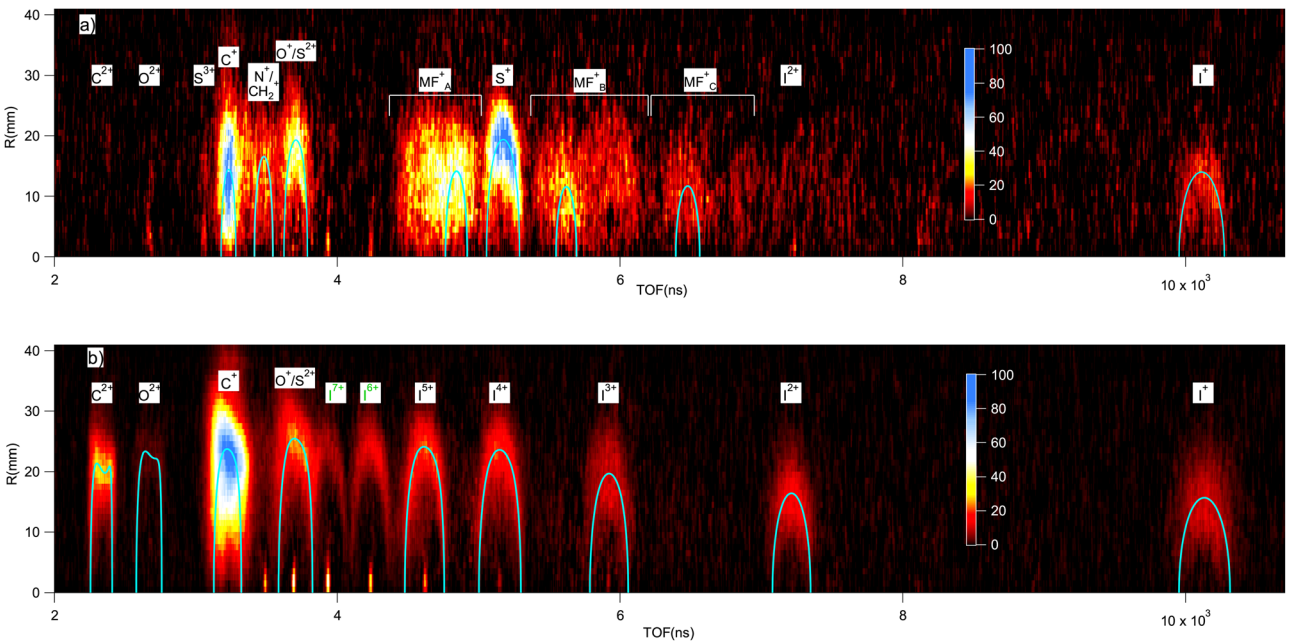

Fig. 5 Ion hit radius R of ion impact positions from the detector center *versus* TOF for ions measured in coincidence with the S 1s (a) and I $2p_{3/2}$ (b) photoelectrons in ISDU. False coincidences were subtracted and the plots slightly smoothed to improve clarity. The blue lines show R(TOF) curves from ray-tracing simulations. Narrow features at small R correspond to I^{n+} ions with near-zero kinetic energy, originating from HI. Ions marked in green arise entirely from I_2 and HI.

In the spectra of ISDU and BrSDU, some expected fragments have equal or nearly equal M/Q ratios: N^+/CH_2^+, O^+/S^{2+} and S^+/I^{4+}. (SI, Section S2). These complications are taken into account when analyzing the data. Additionally, some contaminant ions are present in the data, namely from hydrogen halides and I_2 – their contribution was removed in the analysis (SI, Section S2).

The above analysis deals with single ions in coincidence with the photoelectron. Additional insight into the dissociation paths in the ICE can be provided by ion–ion coincidences, for example by the PEPIPICO maps that in the present case are also utilized for the contaminant subtraction (SI, Section S2). Their usefulness in analyzing the ISDU and BrSDU data is, however, limited, since under the ICE conditions and for the molecules of their size, the momentum correlations of the individual ions are very weak. This results in diffuse, nondescript patterns in the PEPIPICO maps (SI, Fig. S2).

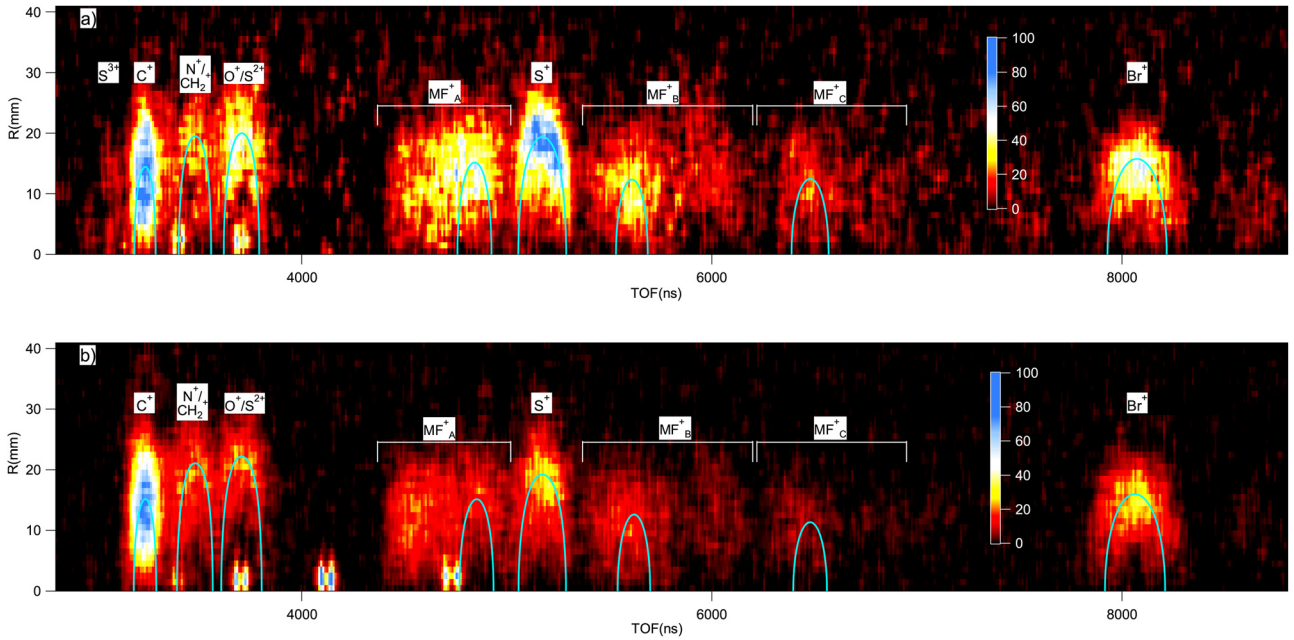

Fig. 6 Ion R(TOF) plots for BrSDU, measured in coincidence with the S 1s (a) and Br $2p_{3/2}$ (b) photoelectrons. The false coincidence map was subtracted and the plots were slightly smoothed to improve clarity. The blue lines show R(TOF) curves from ray-tracing simulations. Sharp features at $R \lesssim 5$ originate from HBr. Region covering the C^{2+} and O^{2+} ions is excluded as only trace amounts were detected.

Table 1 Relative yields of ions observed in coincidence with the I $2p_{3/2}$, Br $2p_{3/2}$ and S 1s photoelectrons in ISDU and BrSDU, normalized to the combined yield of all ions with $M \geq 12$ u (as 100%). The iodine and bromine ions are denoted jointly by X^{n+}. Zero values mark the confirmed absence of the ions, while missing values indicate an overlapping ion/region preventing quantitative analysis of weak signals. Relative yield given for hydrogen is corrected with respect to transmission

				S 1s	
M/Q	Ion	I 2p	Br 2p	ISDU	BrSDU
1	H^+	85	36	23	12
6	C^{2+}	9	0.2	0.2	0.2
8	O^{2+}	1.4	0.1	0.2	0.6
10.7	S^{3+}		0.1	0.8	0.8
12	C^+	53	24	15	14
14	N^+/CH_2^+		8	5	5
16	O^+/S^{2+}	13	9	9	10
32	S^+		13	18	17
~24–30	MF_A^+		17	24	21
~36–46	MF_B^+		11	15	14
~48–58	MF_C^+	0	4	6	6
126.9, 80	X^+	8	13	4	11
63.5, 40	X^{2+}	7		1.9	
42.3, 26.7	X^{3+}	3			
31.7, 20	X^{4+}	2.5	0.2		0
25.4, 16	X^{5+}	3			

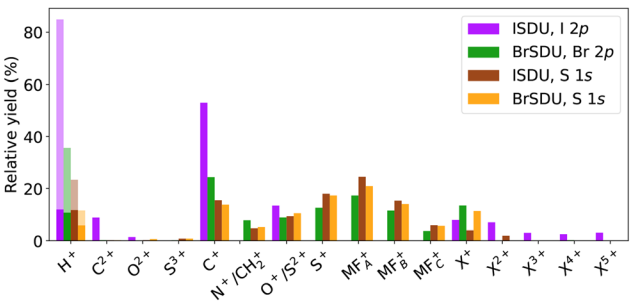

Fig. 7 Relative yields of ions observed in coincidence with the I $2p_{3/2}$, Br $2p_{3/2}$ and S 1s photoelectrons in ISDU and BrSDU, normalized to the combined yield of all ions with $M \geq 12$ u. Shaded areas of the H^+ bars correspond to the increase in the ion yield after transmission correction. Iodine and bromine ions are labeled jointly as X^{n+}.

3.2 Fragment yields

Relative abundances of ions resulting from the photodissociation of ISDU and BrSDU after the I 2p, Br 2p and S 1s ionizations are presented in Table 1 and Fig. 7. The abundances were corrected by removing the contribution of contaminant ions from I_2, HI and HBr, as discussed in the SI.

We conducted a statistical error analysis throughout the various stages of data treatment. The standard deviation by Poisson counting statistics is less than the last reported significant digit in Table 1, and for the high abundances, significantly less. However, other sources of uncertainties limit the accuracy when the statistical error is very small. In addition, the fast hydrogen ions have low transmission, and large errors can be introduced in the correction procedure described in the SI. We estimate the H^+ values in Table 1 to have about 50% error limits; they are also not included in the normalization of total abundances.

The main observations are summarized below; their significance and origin in the photodissociation process will be discussed further in Section 4.2, with the insight from the modeling results.

Different samples: comparing the fragmentation patterns following the S 1s ionization in both samples allows observation of the effect of the different halide substitution in

otherwise identical compounds. The comparison of Fig. 3a, 4a and 7, shows that relative yields of fragments C^+, N^+, O^+ and S^+ and molecular fragments are nearly equal between the samples. Their slightly higher fraction of total yield in ISDU is due to the lower abundance of the I^+ ions as compared to Br^+. This difference has no straightforward explanation in element electronegativities or ionization energies, but we note that the apparent enhancement of the Br^+ yield can also be caused by molecular fragments with the mass of $\approx$80 u, that are indeed produced according to the simulations (see Section 4.1).

Singly charged fragments: the I 2p ionization of ISDU is dominated by the lightest H^+ and C^+ ions, followed by O^+ and I^+. A significant amount of multiply charged species is also present. The estimated final charge here is about +1/3*e* per atom (Section 3.3) and the results show that although it is initiated by a deep localized atomic core hole, it spreads across the molecule prior to the fragment separation.

Nitrogen fragments: a notable feature in the spectrum from I 2p ionization is the clear absence of nitrogen ions N^+, which cannot be obscured by overlapping structures (as is the case for S^+, for example). N^+ is, on the other hand, present following the S 1s and Br 2p ionizations – although it should be noted that the experimentally observed peak at M/Q = 14 u could also be fragment CH_2^+.

Molecular fragments: molecular fragments are not present except for trace amounts after the I 2p ionization, where the higher total charge facilitates a high degree of bond breaks. In contrast, these molecular fragments are clearly visible following the S 1s and Br 2p ionizations.

Doubly charged fragments: carbon C^{2+}, which is a major fragment in the I 2p ionization, is present in trace amounts only after the S 1s and Br 2p ionizations. O^{2+} is seen in trace amounts in all four spectra, with a slightly higher abundance following the I 2p ionization.

Multiply charged fragments: multiply charged iodine fragments are a clear feature in the I 2p ionization. Weak contributions from multiply charged halogen atoms are present in other ionizations as well, although in several cases their quantitative analysis was not possible due to stronger overlapping structures of *e.g.* molecular fragments.

Sulfur fragments: for S^{n+}, charge states up to 3+ were detected. S^+ is prominent following the S 1s (both ISDU and BrSDU) and Br 2p ionization, but in the I 2p ionization, its contribution to the fragmentation pattern is much lower (Fig. 3 and 4). Also, since S^+ strongly overlaps with I^{4+}, the possible minor contribution cannot be quantified. As for S^{2+}, since it is indistinguishable from O^+, its exact abundances cannot be determined accurately. In most cases, it has a lower yield than S^+. Only in the case of the I 2p ionization could S^{2+} yield be higher, which is unlikely since sulfur acquires charge when the Auger cascades spread the positive charge to the entire molecule. There is no apparent reason sulfur atoms would accumulate double instead of a single charge (similarly to the observation of the C^{2+} *versus* C^+ intensity in Fig. 3b). Lastly, trace amounts of S^{3+} were observed in the S 1s ionization of both ISDU and BrSDU (Fig. 3a and 4a).

3.3 Total charge

The ISDU and BrSDU molecules acquire different total charges Q_{tot} following the I 2p, Br 2p and S 1s ionizations. The total released charge could be one of the important metrics when considering, *e.g.*, how the molecule acts as a RS. However, it cannot be directly determined from the measurement of ISDU and BrSDU, as the recorded ions for each event form an incomplete set. Instead, the small contaminant molecules HI, HBr and I_2 now become extremely useful in estimating the total charge. We analyze these compounds (previously filtered out, see SI Section S2) and use literature sources to complement the measured data of ISDU and BrSDU *vis-à-vis* the total charge.

Firstly, as discussed in the SI, in the ion TOF spectra and the R(TOF) plots following the I and Br 2p ionization of ISDU and BrSDU, respectively, we observed sharp peaks corresponding to highly charged I and Br ions of low KE, that were assigned to hydrogen halide molecular dissociation. The average charge of the I^{n+} ions following the I 2p ionization of HI is +6.9*e* (charge distribution given in SI, Section S2.4), and the estimated total charge of HI is +7.9*e*, since the hydrogen fragment most likely also acquires charge. In addition, there are highly charged iodine ions of high KE present in the I 2p-ionized spectra of ISDU, that were unambiguously assigned to the two-body dissociation channels of $I_2^{n+m} \rightarrow (I^{n+}, I^{m+})$. From the abundance analysis of ion pairs in the corresponding region of the PEPIPICO map (SI, Fig. S2), the average total charge of the I_2 molecule was determined to be +9.8*e* (see SI), higher than in HI by +1.9*e*, since the second I atom acts as an additional electron reservoir for the Auger cascade. We use this estimate also for the average total final charge of ISDU following the I 2p ionization, and consequently the SPCHMM model simulations were performed for Q_{tot} = +10*e*.

For the S 1s and Br 2p ionization, equally good internal reference is not available in the data. Molecular dissociation following the S 1s ionization has been studied for the CS_2 and OCS molecules, where the total final charge was found to be +4... +5*e* on average.[50,51] We will use +5*e* in our simulations to represent the outcome of the S 1s ionization. For Br 2p, there is no Br_2 signal for total charge estimation as for I 2p. However, in I_2, Q_{tot} was 1.42 times higher than the average charge of I^{n+} from HI, and assuming the same relationship between Q_{tot} of Br_2 and the average charge of Br^{n+} from HBr (+4.2*e*), we have the estimate of +6.0*e* for Q_{tot} in BrSDU. That was used in model simulations.

Lastly, Ho *et al.* studied core ionization and Coulomb explosion of the IBr molecules and created 2p vacancies *via* radiative decay of the initial 1s vacancy.[10] The resulting Auger cascade then led mainly to +4*e* and +9*e* final charge states in the case of Br and I 2p vacancies, respectively. These values are somewhat lower than our estimates of +6*e* and +10*e*. However, already for HBr our average charge (accounting also for the H^+ ion) is +5.2*e*; it is reasonable that when Br is attached to a larger electron reservoir as in BrSDU, the total charge will only increase.

The above estimates – +10*e* for I 2p, +6*e* for Br 2p and +5*e* for S 1s ionization – are average expected charges, whereas the

charge reached in individual events can vary substantially, as is the case for I_2 (SI, Fig. S3).

3.4 Fragment energies

Both the ion's impact position on the detector and the TOF deviation from the nominal value can be used to determine its momentum and KE.[52] We combined both sources, by comparing the experimental R(TOF) plots with ray-tracing simulations,[15] performed for ions with given mass and charge. We then adjusted the initial KE of the ions until the best visual agreement with the experimental R(TOF) pattern was found. We cross-checked the reliability of the simulations by inspecting the R(TOF)-patterns of the (I^{4+}, I^{5+}) ion pairs from I_2, present in the data from I 2p ionization of ISDU (see SI, Fig. S2). We obtained the kinetic energy release KER = 90 eV and compared it with the value of Posthumus *et al.*,[53] who reported KER = 75.6 eV with multiple ionization using laser pulses of 150 fs duration. Their KER values decrease with the ionizing pulse length, and an extrapolation in accordance with the behaviour of other charge states gives KER $\approx$ 85 eV for 50 fs pulses, approaching well our value of 90 eV for the 0 fs limit.

The resulting simulated R(TOF) curves are plotted in comparison with the experiment in Fig. 5 and 6. In the case of the I 2p ionization, the simulated R(TOF) curves for the fast ions O^{2+} and C^{2+} are distorted due to spherical aberrations in the spectrometer. The diffuse patterns for C^+ ions with broad energy distribution make determining the characteristic energy using best visual agreement more ambiguous, while for other ions the match is more clear. The energies for each ion from each studied ionization are presented in Table 2 and Fig. 8, and will be compared with numerical simulations in Section 4.2, Fig. 9 and 10.

Comparing the experimental results of different ionization edges shows that ISDU and BrSDU exhibit different behavior regarding the KEs of lighter atomic ions, O^+ and C^+, and that of the halogen ion. In ISDU, after the I 2p ionization, the KE of C^+ is 3.5 times that of I^+, but the energies are approximately equal after the S 1s ionization. In BrSDU, the C^+ and Br^+ ions have about the same KE after both the S 1s and Br 2p ionization. Same applies to the O^+ ions – the O^+-to-I^+ ratio changes much more in ISDU than the O^+-to-Br^+ ratio in BrSDU.

As seen in Table 2, the KE could not be determined for the fragments that yielded only trace amounts for some edges, and/or were overlapping with much stronger features. Furthermore, the estimated kinetic energies of the molecular fragments $MF_{A,B,C}^+$ are less reliable than those of the atomic fragments, due to their heavily overlapping R(TOF)-patterns and variability in their mass. However, it can be stated that all the molecular fragments fall in the KE range between 1 to 3.5 eV.

Table 2 Characteristic KEs for ions observed following the I $2p_{3/2}$, Br $2p_{3/2}$ and S 1s ionizations. In addition to undetected fragments, ions with only trace amounts and/or overlapping with stronger peaks in the R(TOF) spectra were not analyzed, and are thus left blank. The iodine and bromine ions are jointly marked by X^{n+}

	Kinetic energy (KE) (eV)			
			S 1s	
Ion	I 2p	Br 2p	ISDU	BrSDU
C^{2+}	31.0			
O^{2+}	30.0			
C^+	10.8	3.4	3.0	3.0
N^+/CH_2^+		7.2	4.0	5.9
O^+/S^{2+}	12.0	8.0	5.6	6.1
S^+		5.4	5.5	5.5
MF_A^+		3.2	2.8	3.2
MF_B^+		2.1	1.8	2.0
MF_C^+		1.7	1.8	2.0
X^+	3.1	3.3	2.4	3.2
X^{2+}	7.1			
X^{3+}	16.5			
X^{4+}	36.0			
X^{5+}	51.0			

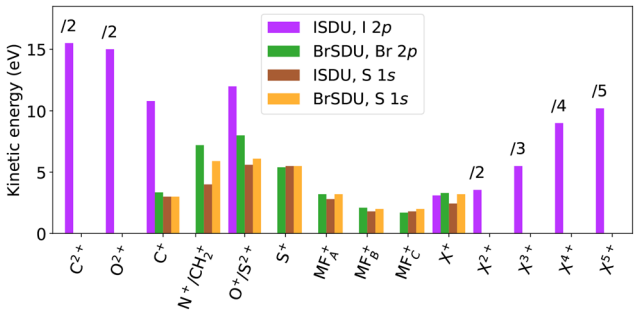

Fig. 8 Characteristic KEs for ions observed following the I and Br $2p_{3/2}$ and S 1s ionization. The energies are scaled by charge for the multiply charged ions. The halogen ions are labeled jointly by X^{n+}.

4 Modeling

To complement the experiment, the Stochastic, Parametric Charge-Hopping Molecular Mechanics (SPCHMM) model was developed in ref. 54 and 55 and is used and developed further here. Comparison with experimental values allows investigation of the model's suitability to describe ICE conditions in such medium-sized biomolecules ($10 \lesssim N_{atoms} \lesssim 100$, $Q_{tot} \ll N_{atoms}$). The model generates statistical data from a large number of FD trajectories, which is directly comparable with the PEPIPICO experiment. It handles efficiently molecular systems comprising tens of atoms, aiming at predicting the outcome of fragmentation rather than detailed evolution of the FD. Next, we will present the essential elements of the model. Readers interested mainly in the outcome of the modeling and how it compares with the experiments are referred directly to Section 4.2.

4.1 Stochastic, parametric charge-hopping molecular mechanics model

The core elements in modeling the fragmentation dynamics by SPCHMM are:

1. Atoms are treated as point charges with integer values (0, $+e$, $+2e$). The total molecular charge $Q_{tot} = +Ne$ can be either allocated to the atoms randomly at $t = 0$, giving a basic representation of the broad range of the electronic final states of the Auger transitions, or built up in a chosen atom from an initial

charge with a linear time constant τ_Q, spreading to the molecule *via* the charge-hopping mechanism. The latter can represent an atomic Auger cascade starting from an inner-shell vacancy.

Simulations for ISDU, ISU, BrSDU and BrSU were run with various total charges Q_{tot} chosen to represent the average charge after the ionization of the I 2p (+10*e*), Br 2p (+6*e*) and S 1s (+5*e*) orbitals (Section 3.3). The charge was initially allocated randomly across the molecule as the baseline approach. Charge build-up and flow from the iodine or bromine atom, although physically justified, was not used in final simulations in this case, as it did not have a major impact on the results and would require additional empirical parameters.

2. The +*e* unit charges can hop across the bonds between atoms during the dynamics at the average hopping frequency f_h. The hops are cut off at a critical distance that depends on the charges of both atoms across the bond and is given by the classical over-the-barrier model.[56] The hops can both increase or decrease the Coulomb potential energy of the whole system, as discussed by Boll *et al.*, for example.[11] On average, there is a tendency of slow cumulative energy gain as a result of the nuclei adapting to the existing point charge distribution between the hops. Such artificial generation of energy, although it can be seen as a model artefact, can be used to represent a gradual internal conversion of energy from the electronic into the nuclear subsystem. In order to control this total energy increase, a directional hop control parameter was introduced. It had a significant influence on the results and therefore we present results from two charge hopping scenarios: the energy-neutral scenario and energy-gain scenario. In both cases, hops are initiated over randomly selected bonds during iteration steps. If the over-the-barrier model allows charge movement in both directions, the direction is chosen randomly in the energy-gain scenario, which results in a slow total energy increase. In the energy-neutral scenario, the hop direction that helps to maintain the total energy is preferred. The difference in probabilities of the two directions is controlled by the hop control parameter, which therefore defines the two scenarios. In the latter scenario, the parameter was tuned to obtain approximately zero net energy gain.

3. The molecular bonds are described by a simplified force field that includes bond stretching and bending. For our purposes, obtaining and maintaining the optimum molecular and fragment geometries is not the primary objective; instead, the force field should be suited for realistic bond breakage description. Morse potential energy curves were chosen to describe the bonds. Bending vibrations were included using a common force constant. Additionally, a force constant can be applied to planar molecules to resist off-plane distortions. No torsional forces were included. As non-bonding interactions, a repulsive potential wall was created around atoms.

4. At the start of the dynamics, the molecule is given internal energy in addition to the potential energy of the Coulomb repulsion of point charges, in the form of randomly distributed atomic velocities (internal temperature). Here, the internal energy of 1 eV per atom was used, representing roughly the broad energy distribution of the electronic states after the Auger cascades.

5. Numerical integration of the FD trajectories was carried out in the molecular system until 1 ps, after which the fragment composition was determined and further fragmentation was excluded. Coulomb explosion was, however, followed until 0.1 ns with the fragments as point charges to accurately include the long-range Coulomb interaction in the final momenta and the KEs of the fragments.

Randomization for the simulated datasets was obtained by (i) choice of the initial atomic velocities, (ii) initial charge localizations, and (iii) redistributing charges across bonds during the hops.

To account for the possibility of thermal decomposition by the breakage of the glycosidic bond, simulations were run for both ISDU and ISU, as well as for BrSDU and BrSU, according to the discussion in Section 1.1 and SI Section S1.

4.2 Simulation results, comparison with experiment

Comparing the experimental results of different ionization edges shows that ISDU and BrSDU exhibit different behaviour regarding the KEs of lighter atomic ions, O^+ and C^+, and that of the halogen ion. At single-ion (noncoincident) level, abundances and KEs of individual fragments are the primary simulation outcomes, and are fully tabulated in the SI. These quantities are mainly, but not entirely, determined by the total charge and internal energy. The average KEs of charged atomic fragments and total KERs from simulated trajectories are shown in Fig. 9 for ISDU and ISU with the total charge of +10*e* (I 2p ionization) and +5*e* (S 1s ionization), and in Fig. 10 for BrSDU and BrSU with Q_{tot} = +6*e* (Br 2p) and +5*e* (S 1s). The KERs show the highest value for ISU (Q_{tot} = +10*e*), as expected since the atomic charges are initially localized in a smaller volume than in ISDU. Simulations with energy-gain-type charge hopping yield higher KERs as a result of the added energy. Experimental KEs are added to Fig. 9 and 10 for the fragments for which they could be reliably determined (Table 2). On the other hand, the KER values cannot be directly compared with experiment. Although Fig. 9 and 10 show only the atomic ions,

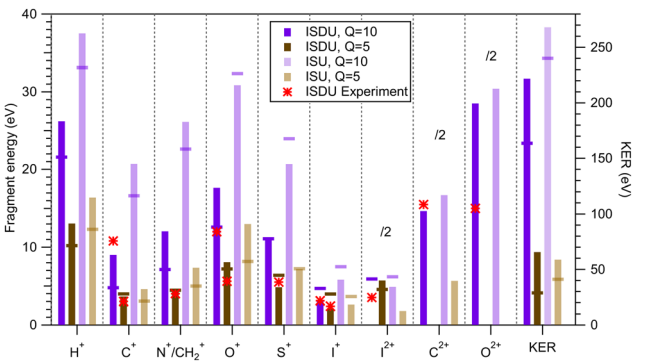

Fig. 9 Kinetic energies of charged atomic fragments and the KER of Coulomb explosion of ISDU and ISU, from SPCHMM modeling. Coloured bars show the results from the energy-gain, and the horizontal markers from the energy-neutral charge-hopping scenarios. Experimental KE's after the I $2p_{3/2}$ and S 1s ionization are given by red markers. Note that the energies of the doubly charged fragments are divided by two.

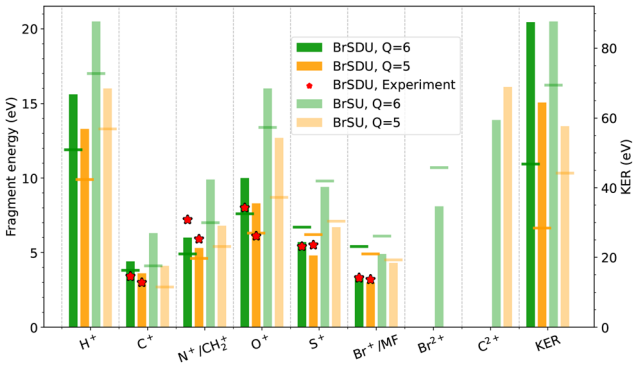

Fig. 10 Kinetic energies of charged atomic fragments and the KER of Coulomb explosion of BrSDU and BrSU, from SPCHMM modeling. Coloured bars show the energy-gain scenario and horizontal markers the energy-neutral scenario. Experimental KEs after the Br $2p_{3/2}$ and S 1s ionizations are given by red markers.

all simulations also produced molecular charged fragments (see SI for details).

The simulations were performed for both the energy-neutral and energy-gain charge hopping, and Fig. 9 and 10 demonstrate that the KEs of atomic ions are quite sensitive to those scenarios, although the relationship is not straightforward. For example, while the KE of the C^+ ions nearly doubles for ISDU, Q_{tot} = 10*e*, when going from the energy-neutral to the energy-gain scenario, the KE of the I^+ ions decreases instead about 1.5 times. The impact on the ion abundances of charge-hopping dynamics can be also quite dramatic, both in ISDU and BrSDU: the yield of the ring atoms C^+, N^+ and O^+ is, in general, strongly reduced under the energy-neutral scenario, while the yield of the peripheral sulfur and halogen ions is increased. This is qualitatively explained, as in the energy-neutral scenario the Coulomb repulsion of the point charges has a steering effect on the charge hopping, tending to localize the positive charge eventually to the peripheral atoms, further from the other charges.

According to the simulations, even the highest charge used, +10*e*: (i) is not sufficient to cause complete atomization of a 28-atom molecule (ISDU), and (ii) creates trajectories of atomic ions that are not representative of the molecular geometry – the momentum correlation of the modelled fragments is similarly diffuse (SI, Fig. S4) compared to that observed in the experiment (SI, Fig. S2). Thus, simulations using the estimated total charges predict ICE conditions for ISDU and BrSDU. Let us further compare the simulation results with the experiment.

For Q_{tot} = +10*e*, a discrepancy with the experiment (I 2p ionization) is seen. In the experiment, only trace amounts of molecular ions were observed, while they constituted about one quarter of the ion yield in simulations of ISDU. Modeling parameters could be a cause of the discrepancy. Firstly, underestimating the total charge for the I 2p ionization – increasing the charge would rapidly reduce the number of intact bonds during the ICE. Using a single charge of +10*e* in simulations is also a simplification, as the actual charge varies event-by-event – for I_2, *e.g.*, total charges up to +14*e* were detected (SI, Fig. S3). Secondly, increasing the integration time beyond 1 ps, the dissociation of the remaining molecular fragments could be continued. Neutral fragments are unobserved in the experiment, and if the molecular fragments produced in the I 2p experiment are predominantly neutral, the discrepancy would be more related to the charge localization than to the degree of atomization.

Pre-ionization rupture of the glycosidic bond would be a possible cause of depletion of the molecular fragments in the experimental spectrum, because the iodine-containing fraction, ISU, would then contain the entire charge and undergo a much more complete CE. Indeed, the simulations predict only a 3–4% yield of the molecular fragments for ISU, Q_{tot} = +10*e*. However, there are also contrary indications to the pre-ionization rupture of the glycosidic bond. Most notably, following the I 2p ionization, the N^+ ions are absent in the experimental spectrum, although there is a strong signal of O^+ – this is not consistent with the $C_4H_3IN_2OS$ composition and full CE of ISU. On one hand, it would be very difficult to construct a simulation scenario for ISU, with +0.83*e* per atom charge, where no or a very low number of N^+ ions are produced – our simulations yielded 0.35–1.12 ions per trace (depending on the charge-hopping scenario, SI, Table S1). On the other hand, N^+ can be produced with a very low yield in simulations for ISDU, *e.g.*, only 0.02 ions per trace for Q_{tot} = 10*e*, energy-neutral scenario (SI, Table S1); a result much closer to the experiment. The I 2p ionization is experimentally dominated by the ejection of the lightest atomic fragments (protons and C^{n+}), which is also the case for simulations with Q_{tot} = +10*e*. These are, naturally, also the prevailing elements in the molecule. In the S 1s ionization experiment, molecular fragments appear. The simulations show (Table S1 in SI) a corresponding increase in the charged molecular fragments of about 1.6 times, when the charge is reduced from +10*e* to +5*e*.

The energy-gain scenario leads to a better overall agreement with the experiment with fewer clear outliers. For example, as pointed out in Section 3.4, the C^+ ions have about 3.5 times higher KE than the I^+ ions in the case of the I 2p ionization. The energy-neutral simulation produces nearly equal KEs of C^+ and I^+, while under the energy-gain scenario, the C^+ ions have three times higher KE. Also for the lower charge state Q_{tot} = +5*e* (the S 1s ionization), the energy-gain scenario agrees better with the experiment than the energy-neutral scenario, although the differences are not as large.

Turning now to the second sample, BrSDU, we see that already in the Br 2p ionization, the measured mass spectrum of BrSDU contains a significant fraction of molecular fragments (Fig. 4b). In a corresponding simulation (Q_{tot} = +6*e*), the charged molecular fragments constitute about one third of the total ion yield (including the light fragment CH_2^+).

For the lower +5*e* total charge, we firstly note that the simulations for both ISDU and BrSDU produced very similar results, as did the corresponding S 1s ionization experiments. The charged molecular fragments are now slightly more abundant in BrSDU, consisting 36–40% of the ion yield. Specific to the case of BrSDU, not all fragments with mass 80 u are Br^+ in

the simulations, but are molecular fragments of the rings, notably a part of the deoxyribose ring. For charge states Q_{tot} = +5e and Q_{tot} = +6e, approximately 34% and 30%, respectively, of the mass-80 u fragments are molecular (under the energy-gain scenario). Regarding mass-14 u ions in BrSDU, initially assigned to the N^+ fragments, in the energy-neutral simulations (Q_{tot} = +5e) these are in fact the molecular fragments CH_2^+, while in energy-gain simulations, they are mostly N^+ (approximately 15% are CH_2^+).

Lastly, we note that in BrSDU, the charge-hopping scenarios influence the yield of the atomic ions similarly to ISDU: under the energy-neutral scenario the charge tends to localize more on the peripheral atoms S and Br, considerably increasing the yield of these ions.

5 RS properties – implications of the present study

Research on radiation damage typically extends to low-energy secondary electrons and hydroxyl radicals formed by water radiolysis while studies on RS drugs tend to be rather empirical and focus on physiological effects of the RS drugs rather than on the involved chemical and physical processes.[20,57–59] However, a better understanding of the fundamental processes can aid in the development of more efficient RS drugs. Our first experimental results with the new coincidence capability of MUSTACHE show the first steps in the radiation damage caused by high-Z RSs absorbing high-energy X-rays. We observed that upon irradiation these RSs undergo violent fragmentation producing Auger and low-energy electrons, high-energy ions and abundant energetic protons – species that are capable of causing localized chemical damage and secondary ionization.

The present isolated-molecule study addressed specifically the direct effect of X-rays interacting with the deep inner atomic shells of ISDU and BrSDU as relevant to the initial steps in the radiation damage, releasing fragments that propagate the damage to the surroundings of the molecule. Results of the I 2p ionization of ISDU, a compound with an observed RS effect,[13] can be seen as most closely related to the effect of medical X-rays. Our experimental results show a high degree of atomization upon I 2p ionization of ISDU, where the atomic carbon and protons dominate the fragment pattern. The estimate for the proton energy, that was obtained combining the experimental data with simulations, is about 22 eV. In total, the released fragments carry about 160–220 eV KE following the I 2p ionization, according to the simulations. In addition to this energy which is deposited in the near surroundings of ISDU, the KE of on average ten electrons is released in the Auger cascade. While the entire electron spectrum was not recorded in this experiment, it has been investigated by theoretical methods by Chaynikov *et al.*[1] They found the main regions of Auger electron emission from atomic iodine to be (i) below 1 keV and (ii) between approximately 2.2 and 5.2 keV. In the case of K-shell ionization, some electron emission also occurs above 20 keV, while the 1s vacancy is filled. These fast electrons and protons would cause substantial secondary ionization in the local environment, to be included in the models of the radiation damage spread.[60–62]

As for the BrSDU that showed no RS properties, the Br 2p ionization leads to about three times smaller KER than in the analogous I 2p ionization of ISDU, according to the simulations. This could be a contributing factor to the observed differences in their RS properties. Also the fragment composition following the ionization of the 2p orbital of bromine in BrSDU is quite different compared to that of iodine in ISDU – relative yield of protons following Br 2p ionization is less than half the yield after I 2p ionization (Table 1 and Fig. 7). Additionally, the KE of the protons released after I 2p ionization is almost twice that of protons from Br 2p ionization, according to simulations (Fig. 9 and 10). The experimental fragmentation pattern for I 2p in ISDU is, in general, dominated by the light fragments, often doubly charged. In contrast, in the Br 2p ionization experiment of BrSDU, the slow molecular fragments, as well as the heavier S^+ atomic fragment, comprise a significant portion of the charged fragments (Fig. 7). These characteristics combined can result in quite a different radiation damage effect of ISDU and BrSDU on the local environment as medical X-ray absorption hotpots.

6 Conclusion

In this work, we characterized the reaction of biologically and therapeutically relevant medium-sized molecules to deep inner-shell ionization, a typical process related to medical X-rays. Experimentally, the outcome of the multi-particle incomplete Coulomb explosion (ICE) was represented primarily as ion yields and KEs. For both ISDU and BrSDU, the experiment quantified the trends as ionization moved towards deeper inner-shells, *e.g.*, the increasing fraction of atomic fragments, larger kinetic energies, and appearance of multiply charged ions. This detailed data allows the development and fine-tuning of numerical models for biomolecules in the ICE regime.

The experiment demonstrated the suitability of the electron-energy-resolved PEPIPICO technique to target specific deep inner-shell ionization edges. In this molecular size range, the technique also shows limitations, and therefore, the data was augmented by molecular mechanics simulations, designed specifically to yield data comparable with the coincidence experiment. The numerical modeling by SPCHMM used here showed that such models can be used to complement the experimental results. At the same time, questions regarding the appropriate coupling of the nuclear and electronic dynamics during the ICE process remain to be fully answered with further help from chosen experimental targets. This study shows that for stochastic point-charge models describing ICE, details of the charge dynamics (*e.g.*, energy-neutral or energy-gain scenarios) can strongly influence the outcome and its agreement with observations. Further comparisons with experimental results on simpler test systems are planned specifically to refine this aspect of the model.

The obtained experimental data is also relevant beyond the single-molecule environment, for example, in modeling near-neighborhood environmental damage caused by the X-ray absorption hotspots ISDU and BrSDU, relevant to the RS properties. An early version of such a model, tracking the diffusion of energy into the local environment by collisions, was tested in the case of soft X-ray ionization by Pihlava *et al.*[63] With the tender X-rays, the energetic atomic ions, including heavy iodine and multiply charged species, may also significantly contribute to local chemical damage beyond that caused by Auger electrons, low-energy electrons, or water-derived reactive species alone. The present study confirms that all these factors are notably emphasized in deep inner-shell ionization of ISDU over BrSDU, which could be responsible, at least partially, for their reported different RS efficiency. On a longer timescale, following the localized Auger cascade, the resulting charge accumulation and proton release into the nearby aqueous environment would modify the surrounding physicochemical conditions, including pH, and influence essential biochemical processes.

Author contributions

Conceptualization: EK, MB, MS, OT; formal analysis: KIP, EK; funding acquisition: EK, MB, MS, OT; investigation: KIP, EK, MB, TM, II, DC, MS, OT; project administration: MS, OT; resources: EK, II, MS, OT; software: EK; supervision: EK, MS; visualization: KIP, EK; writing – original draft: KIP, EK; writing – review & editing; KIP, EK, MB, TM, II, DC, MS, OT.

Conflicts of interest

There are no conflicts to declare.

Data availability

Additional data supporting this article have been included as part of the supplementary information (SI). Supplementary information is available. See DOI: https://doi.org/10.1039/d5cp04872a.

Original data from the coincidence measurements is available from Seafile: https://seafile.utu.fi/d/e766fd60b3b24f95b0c6/.

Acknowledgements

The experiments were performed at the GALAXIES beamline, SOLEIL synchrotron, France (Proposal no. 99240244). The authors are grateful to Sylvain Betoule, and Jean-Pascal Rueff and other staff of the SOLEIL synchrotron for assistance during beamtime, and to Renaud Guillemin for his help during the various stages of the project. The authors also thank Pamela H. W. Svensson for making available molecular dynamics calculations for preliminary model verification. E. K. and O. T. acknowledge support from the COST Action MultiChem (CA20129), funded by the European Cooperation in Science and Technology (COST). K.-I. P. acknowledges the financial support of the Finnish Ministry of Education and Culture through the Quantum Doctoral Education Pilot Program (QDOC VN/3137/2024-OKM-4). O. T. acknowledges funding by the French Agence Nationale de la Recherche (ANR) through the MUSTACHE grant ANR-18-CE30-0015. M. B. acknowledges funding from the Estonian Research Council grant (grant PSG1037) as well as support from the Estonian Ministry of Education and Research (TK210, Centre of Excellence in Sustainable Green Hydrogen and Energy Technologies). The authors acknowledge the use of Microsoft Copilot for literature searches and for minor linguistic refinements.

Notes and references

1 A. Chaynikov, A. Kochur and A. Dudenko, *J. Quant. Spectrosc. Radiat. Transfer*, 2024, **322**, 109024.
2 S. Kučas, A. Momkauskaitė, A. Kynienė, Å. Masys and V. Jonauskas, *J. Quant. Spectrosc. Radiat. Transfer*, 2022, **288**, 108249.
3 A. P. Chaynikov, A. G. Kochur, A. I. Dudenko, I. D. Petrov and V. A. Yavna, *Phys. Scr.*, 2023, **98**, 025406.
4 A. Chaynikov, A. Kochur and A. Dudenko, *J. Electron Spectrosc. Relat. Phenom.*, 2025, **281**, 147554.
5 A. Chaynikov, A. Kochur, A. Dudenko and V. Yavna, *J. Quant. Spectrosc. Radiat. Transfer*, 2023, **310**, 108714.
6 B. Erk, D. Rolles, L. Foucar, B. Rudek, S. Epp, M. Cryle, C. Bostedt, S. Schorb, J. Bozek, A. Rouzee, A. Hundertmark, T. Marchenko, M. Simon, F. Filsinger, L. Christensen, S. De, S. Trippel, J. Küpper, H. Stapelfeldt, S. Wada, K. Ueda, M. Swiggers, M. Messerschmidt, C. Schröter, R. Moshammer, I. Schlichting, J. Ullrich and A. Rudenko, *Phys. Rev. Lett.*, 2013, **110**, 053003.
7 A. Rudenko, L. Inhester, K. Hanasaki, X. Li, S. J. Robatjazi, B. Erk, R. Boll, K. Toyota, Y. Hao, O. Vendrell, C. Bomme, E. Savelyev, B. Rudek, L. Foucar, S. H. Southworth, C. S. Lehmann, B. Kraessig, T. Marchenko, M. Simon, K. Ueda, K. R. Ferguson, M. Bucher, T. Gorkhover, S. Carron, R. Alonso-Mori, J. E. Koglin, J. Correa, G. J. Williams, S. Boutet, L. Young, C. Bostedt, S.-K. Son, R. Santra and D. Rolles, *Nature*, 2017, **546**, 129–132.
8 M. Wallner, J. H. D. Eland, R. J. Squibb, J. Andersson, A. H. Roos, R. Singh, O. Talaee, D. Koulentianos, M. N. Piancastelli, M. Simon and R. Feifel, *Sci. Rep.*, 2020, **10**, 1246.
9 B. Q. Lee, H. Nikjoo, J. Ekman, P. Jönsson, A. E. Stuchbery and T. Kibédi, *Int. J. Radiat. Biol.*, 2016, **92**, 641–653.
10 P. J. Ho, D. Ray, C. S. Lehmann, A. E. A. Fouda, R. W. Dunford, E. P. Kanter, G. Doumy, L. Young, D. A. Walko, X. Zheng, L. Cheng and S. H. Southworth, *J. Chem. Phys.*, 2023, **158**, 134304.
11 R. Boll, J. M. Schäfer, B. Richard, K. Fehre, G. Kastirke, Z. Jurek, M. S. Schöffler, M. M. Abdullah, N. Anders, T. M. Baumann, S. Eckart, B. Erk, A. De Fanis, R. Dörner, S. Grundmann, P. Grychtol, A. Hartung, M. Hofmann, M. Ilchen, L. Inhester, C. Janke, R. Jin, M. Kircher, K. Kubicek, M. Kunitski, X. Li,

T. Mazza, S. Meister, N. Melzer, J. Montano, V. Music, G. Nalin, Y. Ovcharenko, C. Passow, A. Pier, N. Rennhack, J. Rist, D. E. Rivas, D. Rolles, I. Schlichting, L. P. H. Schmidt, P. Schmidt, J. Siebert, N. Strenger, D. Trabert, F. Trinter, I. Vela-Perez, R. Wagner, P. Walter, M. Weller, P. Ziolkowski, S.-K. Son, A. Rudenko, M. Meyer, R. Santra and T. Jahnke, *Nat. Phys.*, 2022, **18**, 423–428.

12 T. Jahnke, S. Mai, S. Bhattacharyya, K. Chen, R. Boll, M. E. Castellani, S. Dold, U. Frühling, A. E. Green, M. Ilchen, R. Ingle, G. Kastirke, H. V. S. Lam, F. Lever, D. Mayer, T. Mazza, T. Mullins, Y. Ovcharenko, B. Senfftleben, F. Trinter, Atia-Tul-Noor, S. Usenko, A. S. Venkatachalam, A. Rudenko, D. Rolles, M. Meyer, H. Ibrahim and M. Gühr, *Nat. Commun.*, 2025, **16**, 2074.

13 S. Makurat, P. Spisz, W. Kozak, J. Rak and M. Zdrowowicz, *Int. J. Mol. Sci.*, 2019, **20**, 1308.

14 P. Spisz, M. Zdrowowicz, S. Makurat, W. Kozak, K. Skotnicki, K. Bobrowski and J. Rak, *Molecules*, 2019, **24**, 2819.

15 E. Kukk, R. Vacheresse, I. Ismail, T. Marchenko, R. Guillemin, M. N. Piancastelli, M. Simon and O. Travnikova, *J. Synchrotron Radiat.*, 2025, **32**, 1017–1027.

16 M. O. Krause, *J. Phys. Chem. Ref. Data*, 1979, **8**, 307–327.

17 A. P. Chaynikov, A. G. Kochur and A. I. Dudenko, *Phys. Scr.*, 2024, **99**, 045407.

18 E. J. Hall and A. J. Giaccia, *Radiobiology for the radiologist*, Wolters Kluwer Lippincott Williams Wilkins, Philadelphia, PA, 7th edn, 2012, ch. 1, pp. 9–10.

19 H. Wang, X. Mu, H. He and X.-D. Zhang, *Trends Pharmacol. Sci.*, 2018, **39**, 24–48.

20 J. Rak, L. Chomicz, J. Wiczk, K. Westphal, M. Zdrowowicz, P. Wityk, M. Żyndul, S. Makurat and Å. Golon, *J. Phys. Chem. B*, 2015, **119**, 8227–8238.

21 K. Westphal, J. Wiczk, J. Miloch, G. Kciuk, K. Bobrowski and J. Rak, *Org. Biomol. Chem.*, 2015, **13**, 10362–10369.

22 G. H. Hitchings, E. A. Falco and M. B. Sherwood, *Science*, 1945, **102**, 251–252.

23 H. Abdoul-Carime, P. Limão-Vieira, S. Gohlke, I. Petrushko, N. J. Mason and E. Illenberger, *Chem. Phys. Lett.*, 2004, **393**, 442–447.

24 R. Brem, X. Zhang, Y.-Z. Xu and P. Karran, *J. Photochem. Photobiol., B*, 2015, **145**, 1–10.

25 G. Wenska, K. Taras-Goślińska, B. Skalski, G. L. Hug, I. Carmichael and B. Marciniak, *J. Org. Chem.*, 2005, **70**, 982–988.

26 S. J. Karnas, E. Yu, R. C. McGarry and J. J. Battista, *Phys. Med. Biol.*, 1999, **44**, 2537–2549.

27 M. Y. Ye and Y. Shen, *J. Liq. Chromatogr.*, 1994, **17**, 773–791.

28 P. Bolognesi, M. Castrovilli, P. O'Keeffe, A. Casavola, D. Catone, S. Turchini and L. Avaldi, *Nucl. Instrum. Methods Phys. Res., Sect. B*, 2012, **279**, 118–123.

29 W. H. Prusoff, M. S. Chen, P. H. Fischer, T.-S. Lin, G. T. Shiau, R. F. Schinazi and J. Walker, *Pharmacol. Therapeutics*, 1979, **7**, 1–34.

30 D. S. Shewach and T. S. Lawrence, in *Nucleoside Radiosensitizers*, ed. G. J. Peters, Humana Press, Totowa, NJ, 2006, pp. 289–329.

31 Y.-Z. Xu, X. Zhang, H.-C. Wu, A. Massey and P. Karran, *Bioorg. Med. Chem. Lett.*, 2004, **14**, 995–997.

32 X.-H. Zhang, H.-Y. Yin, G. Trigiante, R. Brem, P. Karran, M. B. Pitak, S. J. Coles and Y.-Z. Xu, *Chem. Lett.*, 2014, **44**, 147–149.

33 X. Zhang and Y.-Z. Xu, *Molecules*, 2011, **16**, 5655–5664.

34 M. Zdrowowicz, P. Spisz, A. Hać, A. Herman-Antosiewicz and J. Rak, *Int. J. Mol. Sci.*, 2022, **23**, 1429.

35 F. Izadi, A. Szczyrba, M. Datta, O. Ciupak, S. Demkowicz, J. Rak and S. Denifl, *Int. J. Mol. Sci.*, 2023, **24**, 8706.

36 M. Saqib, E. Arthur-Baidoo, F. Izadi, A. Szczyrba, M. Datta, S. Demkowicz, J. Rak and S. Denifl, *J. Phys. Chem. Lett.*, 2023, **14**, 8948–8955.

37 E. Itälä, D. T. Ha, K. Kooser, E. Rachlew, M. A. Huels and E. Kukk, *J. Chem. Phys.*, 2010, **133**, 154316.

38 K. Nagaya, K. Motomura, E. Kukk, H. Fukuzawa, S. Wada, T. Tachibana, Y. Ito, S. Mondal, T. Sakai, K. Matsunami, R. Koga, S. Ohmura, Y. Takahashi, M. Kanno, A. Rudenko, C. Nicolas, X.-J. Liu, Y. Zhang, J. Chen, M. Anand, Y. Jiang, D.-E. Kim, K. Tono, M. Yabashi, H. Kono, C. Miron, M. Yao and K. Ueda, *Phys. Rev. X*, 2016, **6**, 21035.

39 K. Nagaya, K. Motomura, E. Kukk, Y. Takahashi, K. Yamazaki, S. Ohmura, H. Fukuzawa, S. Wada, S. Mondal, T. Tachibana, Y. Ito, R. Koga, T. Sakai, K. Matsunami, K. Nakamura, M. Kanno, A. Rudenko, C. Nicolas, X.-J. Liu, C. Miron, Y. Zhang, Y. Jiang, J. Chen, M. Anand, D. E. Kim, K. Tono, M. Yabashi, M. Yao, H. Kono and K. Ueda, *Faraday Discuss.*, 2016, **194**, 537–562.

40 S. M. Hecht, A. S. Gupta and N. J. Leonard, *Biochim. Biophys. Acta, Nucleic Acids Protein Synth.*, 1969, **182**, 444–448.

41 M. S. Robinson, M. Niebuhr and M. Gühr, *Molecules*, 2023, **28**, 2354.

42 B. Roy, E. Titov, M. S. Robinson, M. Gühr and P. Saalfrank, *J. Phys. Chem. A*, 2025, **129**, 7352–7364.

43 H. Levola, K. Kooser, E. Itälä and E. Kukk, *Int. J. Mass Spectrom.*, 2014, **370**, 96–100.

44 E. Itälä, K. Kooser, E. Rachlew, H. Levola, D. T. Ha and E. Kukk, *J. Chem. Phys.*, 2015, **142**, 194303.

45 E. Itälä, M. A. Huels, E. Rachlew, K. Kooser, T. Hägerth and E. Kukk, *J. Phys. B: At., Mol. Opt. Phys.*, 2013, **46**, 215102.

46 H. Levola, K. Kooser, E. Rachlew, E. Nommiste and E. Kukk, *Int. J. Mass Spectrom.*, 2013, **353**, 7–11.

47 O. González-Magaña, M. Tiemens, G. Reitsma, L. Boschman, M. Door, S. Bari, P. O. Lahaie, J. R. Wagner, M. A. Huels, R. Hoekstra and T. Schlathölter, *Phys. Rev. A: At., Mol., Opt. Phys.*, 2013, **87**, 032702.

48 P. H. W. Svensson, B. Rydgren, L. Schwob, M. Berholts, B. Stenerlöw, O. Hocine Hafiani, T. André, O. Grånäs, N. Timneanu, J. Leroux, A. Nair, L. Pille, B. Oostenrijk, S. Bari, O. Björneholm and C. Caleman, *Chem. Sci.*, 2025, **16**, 19235–19243.

49 J.-P. Rueff, J. M. Ablett, D. Céolin, D. Prieur, T. Moreno, V. Balédent, B. Lassalle-Kaiser, J. E. Rault, M. Simon and A. Shukla, *J. Synchrotron Radiat.*, 2015, **22**, 175–179.

50 O. Grånäs, A. Mocellin, E. S. Cardoso, F. Burmeister, C. Caleman, O. Björneholm and A. N. De Brito, *J. Phys. B: At., Mol. Opt. Phys.*, 2020, **53**, 244007.

51 B. Esser, U. Ankerhold, N. Anders and F. V. Busch, *J. Phys. B: At., Mol. Opt. Phys.*, 1997, **30**, 1191–1206.

52 E. Kukk, *J. Phys. B: At., Mol. Opt. Phys.*, 2025, **58**, 065101.

53 J. H. Posthumus, A. J. Giles, M. R. Thompson and K. Codling, *J. Phys. B: At., Mol. Opt. Phys.*, 1996, **29**, 5811–5829.
54 E. Kukk, H. Myllynen, K. Nagaya, S. Wada, J. D. Bozek, T. Takanashi, D. You, A. Niozu, K. Kooser, T. Gaumnitz, E. Pelimanni, M. Berholts, S. Granroth, N. Yokono, H. Fukuzawa, C. Miron and K. Ueda, *Phys. Rev. A*, 2019, **99**, 023411.
55 E. Kukk, L. Pihlava, K. Kooser, C. Stråhlman, S. Maclot and A. Kivimäki, *Phys. Chem. Chem. Phys.*, 2023, **25**, 5795–5807.
56 R. Boll, B. Erk, R. Coffee, S. Trippel, T. Kierspel, C. Bomme, J. D. Bozek, M. Burkett, S. Carron, K. R. Ferguson, L. Foucar, J. Küpper, T. Marchenko, C. Miron, M. Patanen, T. Osipov, S. Schorb, M. Simon, M. Swiggers, S. Techert, K. Ueda, C. Bostedt, D. Rolles and A. Rudenko, *Struct. Dyn.*, 2016, **3**, 043207.
57 B. Jones and R. G. Dale, *Br. J. Radiol.*, 2018, **92**, 20180097.
58 L. L. Gardner, S. J. Thompson, J. D. O'Connor and S. J. McMahon, *Phys. Med. Biol.*, 2024, **69**, 18TR01.
59 S. J. McMahon and K. M. Prise, *Cancers*, 2019, **11**, 205.
60 D. Céolin, J.-P. Rueff, A. Zimin, P. Morin, V. Kimberg, S. Polyutov, H. Ågren and F. Gel'mukhanov, *J. Phys. Chem. Lett.*, 2017, **8**, 2730–2734.
61 V. C. D'mello, V. R. Mundlapati, J. Donon, V. Brenner, M. Mons, D. Céolin and E. Gloaguen, *Chem. Sci.*, 2025, **16**, 21041–21046.
62 J. Hofierka and L. S. Cederbaum, *Radiat. Phys. Chem.*, 2026, **239**, 113343.
63 L. Pihlava, P. H. W. Svensson, E. Kukk, K. Kooser, E. De Santis, A. Tõnisoo, T. Käämbre, T. André, T. Akiyama, L. Hessenthaler, F. Giehr, O. Björneholm, C. Caleman and M. Berholts, *Phys. Chem. Chem. Phys.*, 2024, **26**, 8879–8890.